

RESEARCH

Open Access



Air ionization in self-neutralizing air-breathing plasma thruster

Anmol Taploo*, Li Lin and Michael Keidar

*Correspondence:
anmol035@gwu.edu

Micro Propulsion
and Nanotechnology Laboratory,
Department of Mechanical
and Aerospace Engineering,
George Washington University,
Washington DC 20052, USA

Abstract

The paper describes an arc electron source for air ionization applications in a self-neutralizing air-breathing plasma thruster. The arc electron source is an electron source with a prominent level of electron energy control that is required for the air-breathing plasma thruster. The mean energy of the electrons in the arc electron source is controlled by changing the grid voltage in the range of 0V–300V. The Langmuir/Faraday probes were used to obtain ion/electron current, electron temperature, and electron density as a function of pressure and electron energy. Ion current measurements concerning distance from the source were obtained as a function of pressure and grid voltage. Optical emission spectroscopy was used to obtain electron temperature, spectral intensities, and ion formation rate. Additionally, a drift tube based on radial magnetic field electron confinement was designed to detect the presence of negative ions. It has been shown that both positive and negative ions can be produced thus providing conditions for a self-neutralizing air-breathing plasma thruster.

Keywords: Air-breathing, Diagnostics, Plasma chemistry, Negative ion, Neutralization

Introduction

Recently, there has been a growing interest in the research and development of propulsion devices for very low earth orbits [1–3]. These devices would typically function with a thrust level of about 90 mN–90 N to counteract drag level (60 mN– 60 N) in 80 km–260 km altitude ranges [1–3]. The air-breathing plasma thruster would operate by in situ air propellant ionization to produce thrust in these altitudes. This device brings advantages such as low launch cost, payload reduction by eliminating propellant tanks, effective utilization of space resources, and enhanced imaging capability [1]. However, there are some physical and operational challenges, such as developing an optimum approach to air ionization in a rarefied gas environment and building collimator-less designs (collimators introduce additional drag). In their study for ESA's GOCE mission, Wallace, Jameson, and Saunders [4] mentioned that the thrust required appeared lower than anticipated for flying at this altitude. Ferrato, Giannetti, and Piragino's [2] RAM electric propulsion study for air-breathing plasma engines evokes the current design performance limitation of air-breathing plasma engines as unable to produce positive

thrust. The maximum thrust it could provide was about 6 mN, but the drag was almost 26 mN.

Recently it was proposed to use scramjet type configuration without air collimation [1, 3]. In a scramjet type configuration, the incoming air is at a high speed that is not decelerated, unlike with a ramjet. This configuration could potentially eliminate the complexity of using a collimator (which increases the pressure and reduces the velocity) and reduces drag. Typically, an air-breathing plasma thruster would require an external neutralizer to inject electrons for ion beam neutralization. Whereas we propose a self-neutralizing air-breathing plasma thruster (SABPT) design that utilizes positive and negative ions to achieve beam neutralization [1]. Earlier [1], it was shown theoretically that the SABPT has the potential to achieve self-neutralization by operating in a high to low electron energy mode operation. The ions generated inside the thruster could be extracted using electrodes with alternating potential (based on the polarity of the ion charge to extract [1]). As a result, the charge densities would cancel out to achieve a self-neutralized beam. To achieve the design requirements, the electron source inside the SABPT would need to have prominent control over the electron energy for the generation of positive and negative ions. Additionally, its operation would require stability in harsh air plasma environments. To that end, we propose a low-power vacuum arc electron source as a potential electron source to fulfill the SABPT [1] design requirements.

The vacuum arc technology has been studied starting from the nineteenth century. Gilmour and Lockwood [5] conducted experiments to create vacuum arcs with various cathode materials for small propulsion systems with high power densities while simultaneously utilizing magnetic fields to focus the plasma jet. Zhuang et al. [6] and Keidar et al. [7] developed vacuum arc thrusters for the phone sat project at NASA Ames research center and BRIC-Sat CubeSat for US Air Force. Authors [8] also developed an integrated compact magnetic field design for the thrusters. In ion sources, the article [9] describes the development of plasma cathode electron guns using hollow anode and arc discharges. Vacuum arc thrusters exhibit the possibility of multimodal operation [10]. Based on the previous work on the vacuum arcs and electron sources, we propose an arc electron source for the SABPT. The arc electron source (AES) has numerous advantages such as ease of design, long lifetime, ability to work in harsh plasma environments (vacuum-medium pressure range), does not require a separate gas flow rate, utilizes its cathode as a plasma source, and stable operation in pulsed regime while consuming less power. In conclusion, to avoid propellant storage and complicated designs, AES air ionization with self-neutralization capabilities for SABPT can be incorporated.

Earlier, it was mentioned that AES would require a prominent control over electron energy to be utilized as a suitable electron source for SABPT design. To that end, AES consists of an electron extraction grid (Fig. 1(b)). The grid is positively biased to extract the electrons from the vacuum arc plasma. The increase in bias on the grid results in the increment of the mean electron energy. The high energy would result in greater positive ion density, while the low electron energy mode causes negative ion generation (dissociative electron attachment [12]). The electron current is a function of electron drift velocity, so an increase in grid voltage increases electron current. However, electron extraction is disrupted at exceedingly high voltages and pressure due to arcing as the AES operation lands up to the Paschen curve [13]. The increase

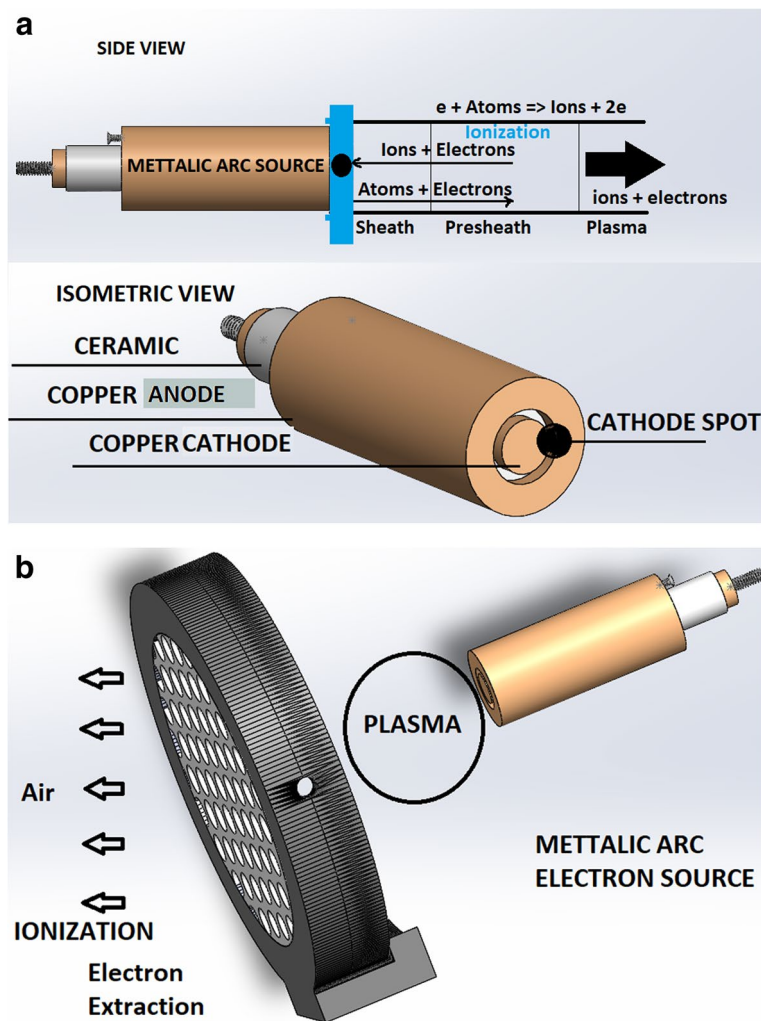


Fig. 1 Schematics of an AES show the vacuum arc plasma source (a) comprising of cathode, anode, and the ceramic gap. The highly concentrated electric field forms between the gaps to initiate a cathode spot [11]. **b** Placement of an electron extraction aluminum grid in the vicinity of the source. The energy of the extracted electrons is controlled by varying the electric potential of the grid. The electrons are removed due to the electric field formed between the vacuum arc source and the grid

in the electron energy results in enhanced collisions with neutral air atoms, thereby causing ionization. The ionization rate (electron density/neutral density) increments with the grid voltage (mean electron energy) like the observation in Ref. [1]. Simultaneously, at lower energies (less than 4 V), O^- ion density is more significant than positive charge density as the attachment dominates the ionization rate coefficient [1]. The schematics of air ionization using AES are shown in Fig. 1(a) and (b). The design (Fig. 1(b)) is divided into the source (behind the grid) and the air ionization region (above the grid). The source segment (Fig. 1(a)) shows the electron emission, ionization, and charge diffusion mechanisms. A small portion of ions returned to the surface after ionization, causing heating and generation of cathode spots. Later, we prove that the AES can generate both positive and negative ions by operating at high and low energy (voltages).

This paper characterizes AES for air ionization applications in a SABPT. The experimental data presented here demonstrate the generation of positive and negative ions. The diagnostics methods such as Langmuir/Faraday probe, optical emission spectroscopy (OES), and magnetic filter to measure negative ion current was utilized to characterize the air plasma. The Langmuir/Faraday probes were used to obtain ion/electron current, electron temperature, and electron density as a function of pressure and electron energy. Ion current measurements concerning distance from the source were obtained as a function of pressure and grid voltage. Optical emission spectroscopy was used to estimate the electron temperature, electron density, and electron energy distribution. Lastly, a magnetic filter was designed/tested to analyze the presence of negative ion current in the air plasma.

Design and characterization of AES for air ionization

The primary focus of this paper is to characterize air ionization using AES. This study also suggests that by modulating the energy of AES and as such forming positive and negative ions, a low-power self-neutralizing SABPT can be achieved. Figure 1(a) shows a vacuum arc source, a copper anode, cathode, and non-porous alumina ceramic. The cathode spot is formed on the ceramic between the cathode and anode. This cathode spot can rotate under the influence of axial magnetic field in J (current density) $\times B$ (magnetic field) motion [14].

A complete electron source comprising a vacuum arc source and the electron extraction grid can be observed in Fig. 1(b). The extraction grid is positively biased with respect to the ground. The extracted electron current and energy are the function of applied grid potential. The electron current extracted saturates at some applied voltage. A typical electron source (hollow cathode) would require a vacuum environment, a thermionic emitter heating system, and a separate propellant tank for its application. In this research, we have shown that our AES does not require those systems. Most importantly, AES can efficiently operate in the medium pressure range (10^{-4} Torr – 10^{-1} Torr). The main objective is to utilize negative ions and positive ions created in the ionization process using AES leading to an extracted neutralized beam at the exit of SABPT. Both negative and positive ions will be accelerated by appropriate electric field arrangement and switching electrodes' polarity [1].

This paper describes the AES using intrusive and non-intrusive plasma diagnostics methods. Figure 2. shows the schematics for the system design configuration starting with an inductive energy storage circuit [15] to power the AES. The inductance, capacitance, switch, input DC voltage, PWM (pulse width modulation) width, frequency, and the coil magnetic field values were $550 \mu\text{H}$, $6800 \mu\text{F}$, IXYH50N120C3D1 IGBT, 30 V, $610 \mu\text{s}$, 5 Hz, and 0.15 T. During the stage 1, the IGBT gate was closed, and high emf is generated in the inductor as it charges.

The gate was open in the second stage, and the stored inductor energy was discharged into the vacuum arc source. With the addition of a capacitor, the overall discharge current was increased. The radius and length dimensions for the cylindrical cathode, anode, and ceramic are 5.5 mm and 40 mm, 6.5 mm and 35 mm, and 12.5 mm and 30 mm, respectively. These dimensions were chosen tentatively as our primary focus is studying ionization and optimization. The ceramic was thin enough

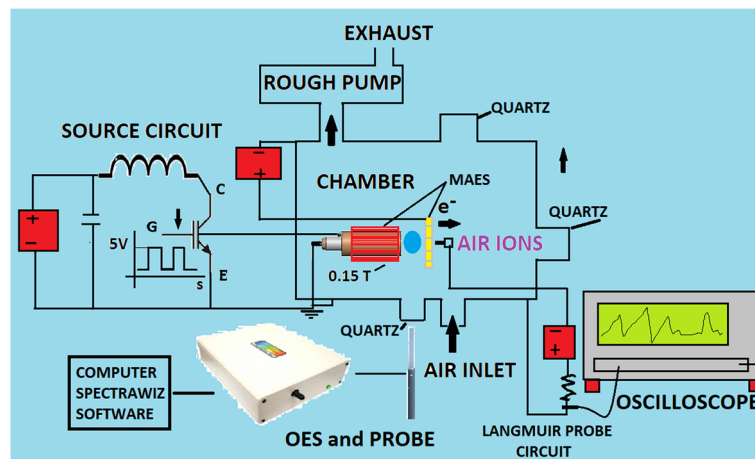


Fig. 2 The schematics of the plasma diagnostics for AES have been described. The diagnostics methods for ion current measurements and OES are displayed. The signals are obtained over the oscilloscope. The plasma chamber was grounded for all the experiments

for a good conduction gap and required a thin carbon paint layer [16] ($100\ \Omega - 200\ \Omega$ resistance between cathode and anode) to ignite the arc. The electron extraction grid is an aluminum grid aperture (diameter 4 mm for each opening) placed on a 50 mm diameter 3D printed extraction grid holder. The aperture was 25 mm away from the source to avoid arcing. The chamber was pumped down using a roughing pump to reach a base pressure of 0.05 Torr. An air leak allowed for a small air flow rate into the chamber. A Langmuir probe with a 2 mm wire length was placed in front of the grid for Langmuir probe experiments. A Faraday cup made up of aluminum was used for ion current measurements. For OES, a Stellar Net Inc. [17] OES spectrometer was coupled with an optical probe placed close to the quartz viewing port of the chamber. The SpectraWiz software was used on the PC to monitor the spectrum. Lastly, the magnetic filter (to measure negative ions) was designed for a length and diameter of 50 mm and 14 mm with a magnetic field of 0.12 T using Alnico permanent magnets (diameter and height as 22 mm and 8 mm).

Optimization using magnetic field

We designed and added an air-cored coil axial magnetic field of 0.15 T to the vacuum arc source to improve the performance. The magnet system does not require an external circuit, and it can be easily integrated into the source. The addition of a magnetic field causes cathode spot rotation [6, 14] and uniform cathode erosion at the cathode-ceramic interface to improve the performance of the source.

Additionally, plasma bends in the $\mathbf{J} \times \mathbf{B}$ direction leading to improvement in ionization, causing an increment in the plasma density and velocity. The ionization in the source was improved with an increase in the magnetic field. The goal was to obtain the optimum magnetic field condition for AES such that the air ion/electron current was maximized. An air-cored coil magnetic field was simulated in FEMM software [18], as shown in Fig. 3(a). An axisymmetric time-invariant field equations model was

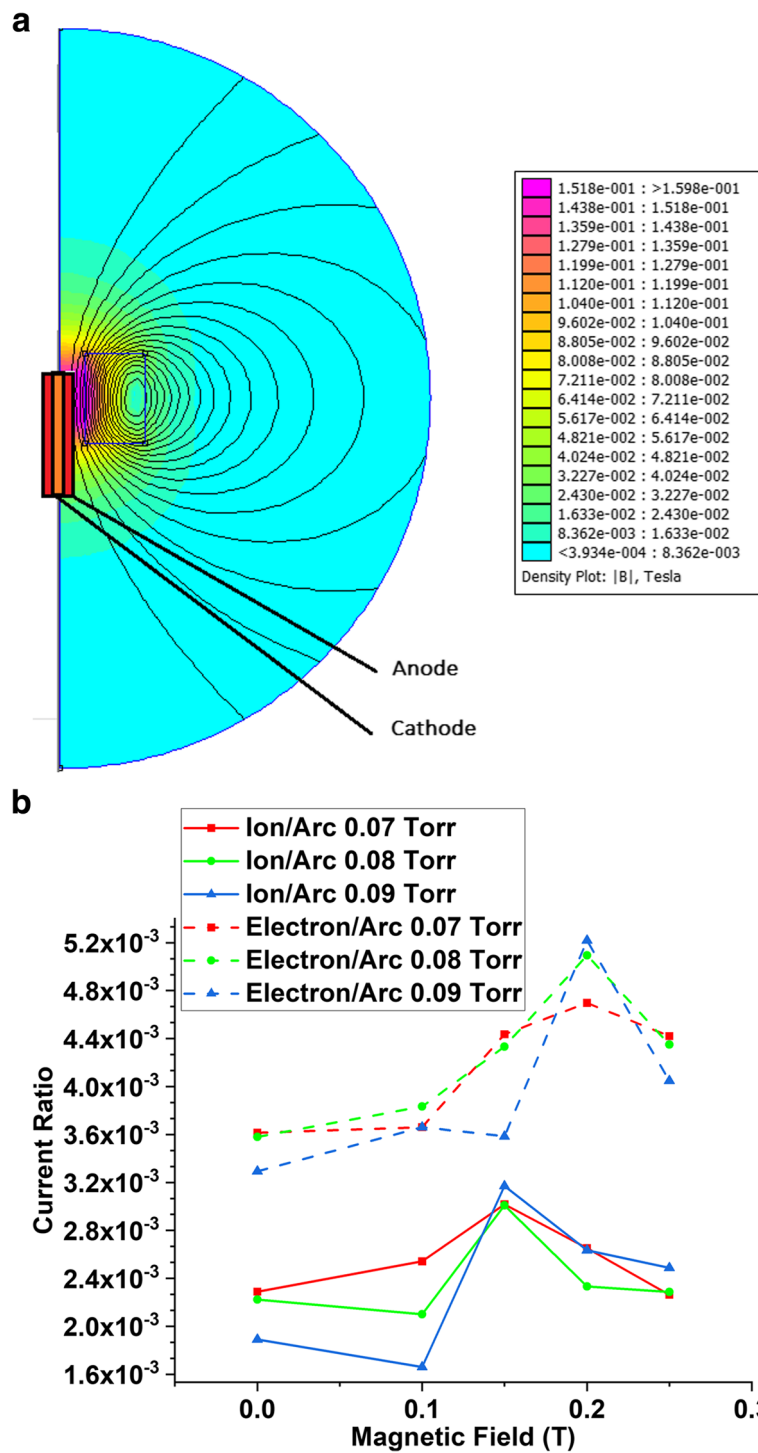


Fig. 3 FEMM Magnetostatics simulation for air-cored coil magnet (a), current ratio vs. magnetic field when the distance between source and Faraday cup is 35 mm (b)

simulated with input conditions of the number of turns, wire gauge, input current, coil radius, and height as sixty-eight turns, AWG 24, 36 A, 12.5 mm, and 13 mm. A peak magnetic field of around 0.15 T can be observed in the middle of the core.

Air ion and electron current experiments were performed at different pressures concerning applied magnetic field 0 T–0.25 T. As observed in Fig. 3(b), the 0.15 T–0.2 T field showed peak performance, but 0.15 T was chosen. Ion and electron currents were measured using an Aluminum Faraday cup (diameter 56 mm) placed 35 mm away from the source by biasing it – (for ions)/+ (for electrons) 40 V. The magnetic field significantly increased the ion and electron/arc current ratio. Beyond 0.2 T, there is a reduction in ion or electron/arc current ratio; this is likely due to electron confinement leading to disruption of the arc current.

Langmuir probe and faraday cup

The Faraday cup experiments were performed using a cup area of 0.03 m². The current was calculated using Ohm's law for a potential drop across a 100 Ω resistor. Additionally, the Langmuir probe was built with a titanium wire for thickness and length of 1 mm, and 2 mm exposed to the plasma (the remaining was shielded using a non-porous alumina ceramic). Results have been presented in section 3.1.

Optical emission spectroscopy (OES) and plasma chemistry

The OES technique gave an insight into plasma chemistry by studying the emissions in the visible spectrum. The emission lines are interpreted from the NIST database [19] for atoms and the molecular spectra book [20] for molecules. The results of OES can also assist in understanding plasma chemistry. The electron temperature, electron density, and energy distribution function parameters could be calculated. The natural logarithmic eq. (1) is based on two selected line spectrums [21, 22]

$$\ln\left(\frac{\lambda_i I_i}{A_i g_i}\right) = \frac{-E_i}{k_B T_e} + Constant \quad (1)$$

Here i , I , λ , A , g , k_B , T_e , and E are spectral line number, spectral line intensity, wavelength (nm), transmission probability, statistical weight, Boltzmann constant ($1.38 \times 10^{-23} \text{ m}^2 \text{ Kg s}^{-2} \text{ K}^{-1}$), electron temperature (eV) and energy (eV). The eq. (1) mentioned above can be curve fitted to obtain electron temperature. When plugged into the ion saturation current equation from the Langmuir probe, the electron temperature can give electron density. Alternately, the Saha equation (Ref. [22, 23]) could also be used to obtain electron density. The above equations are based on the local thermodynamic equilibrium (LTE) condition. The vacuum arc sources have EEDF (electron energy distribution function) in the Maxwellian regime [22] due to LTE and high collision frequency. This condition can be used for our case because the incoming airflow is exceptionally low density. The next step is to obtain the reaction rate coefficient for attachment and ionization reactions. The rate coefficients can determine the rate of positive and negative ions formation based on the plasma chemical reactions and their transport coefficients [24]. The rate coefficient is given by [25, 26],

$$k_k = \sqrt{\frac{2.5477e}{m_e}} \int_0^\infty \sigma_k(\varepsilon) \varphi^{-1.5} \varepsilon e^{\left(\frac{-\varepsilon}{\varphi}\right)} d\varepsilon \quad (2)$$

Here, e , ε and ϕ , m_e , and $\sigma_k(\varepsilon)$ are electron charge, electron energy (eV) and mean electron energy (eV), the mass of the electron (9.1×10^{-31} Kg), and electron impact collisional cross-sections (m^2). The formation rate for specific reactions can be obtained by multiplying rate coefficients with their respective reactants' number densities. The above eqs. 1 and 2 consider LTE. The Boltzmann equation shall be solved in the case of non-Maxwellian distribution (non-thermal plasma) because the Boltzmann transport equation assumes the effect of the inelastic collision. It is computationally expensive. A Boltzmann solver can be used to compute EEDF [24, 27] when the EEDF distribution is non-Maxwellian. The GUI of the solver takes input as a collision cross-section database which can be obtained from the LXcat [28] website. The other inputs are gas temperature, ionization degree, plasma density, mean electron energy, and electric field by number density ratio to compute rate and transport coefficients. Additionally, EEDF and rate coefficients can provide adequate knowledge of plasma chemistry. Hence, we use it to verify the ion formation concerning our parameters, such as extraction grid voltage and pressure.

Magnetic filter design

The negative charge in the air plasma is a blend of electrons and negative ions (O^- is dominant [29]). These charges can be differentiated based on their mass, gyro radius, and velocity (distance/delay time). The O^- ions are typically formed at lower energies due to the dissociative attachment process. However, the ions get destroyed mainly because of electron impact detachment or mutual neutralization with O^+ and O_2^+ ions [30]. Therefore, researchers have attempted to measure and study negative oxygen ions using the experimental and modeling approach. For instance, McKnight [31] investigated drift velocities and rate constants for negative oxygen (in oxygen plasma) ions experimentally as a function of electric field-neutral density ratio, pressure, and gas temperature, to verify the calculations with their numerical results. In the field of helicon wave discharge, Mieno et al. [32] experimentally studied negative and positive oxygen ions formation in an oxygen plasma due to rf (radio frequency) power modulation (on-off power) using a time-of-flight mass spectrometer. Additionally, Zhang et al. [33] used a floating harmonic method to investigate negative ion density and electronegativity variation with the radial distance, gas pressure, and power in an inductively coupled plasma. Regarding a mathematical model, the authors [34] obtained a temporal variation of negative ion density by solving a 1D hydrodynamic drift model (motion of charges, ionization, and recombination reactions in a spatial-temporal varying electric field). While most works were conducted for an electronegative gas (O_2) plasma, the research lacked experimental negative oxygen ion data for air plasma.

To this end, we propose an approach based on partial magnetization through magnetic field confinement of electrons. The negative ions drifting towards the probe will allow ion current measurement. The magnetic filter length was decided based on the criteria that the dimension (L_{Tube}) was selected between the range of Larmor radius for negative ions and electrons. This condition permitted effective electron confinement while ensuring negative ions drift towards the current measuring electrode 2. The measuring tube design system was electrically floating to prevent positive ions

from entering electrode 1 (due to the potential difference between electrode 1 and the ground). The length of the tube was inversely related to the applied magnetic field.

The tube design is guided by partial magnetization condition:

$$\frac{m_e}{eB} \left(\sqrt{\frac{2U_{Battery}e}{m_e} + u_e^2} \right) < L_{Tube} < \frac{m_i}{eB} \left(\sqrt{\frac{2U_{Battery}e}{m_i} + u_i^2} \right) \tag{3}$$

where m_i , $U_{Battery}$, u_e , u_i and B are oxygen ion mass (2.65×10^{-26} Kg), applied voltage, initial electron, initial ion velocity (ratio of the distance between AES-tube and delay time), and the applied magnetic field using Alnico permanent magnet (0.12 T). Based on eq. 3, a tube length of 50 mm for an applied, voltage of 80 V was selected for the experiments such that electrons were radially confined, and the negative ions were not magnetized. The applied voltage results in an electric field between the plasma, electrodes 1 and 2 (Fig. 4) extracting the negative charges (electrons and negative ions) as they move from low to high potential, simultaneously repelling the positive charge. Electrons are confined radially using the radial magnetic field. Even though a strong magnetic field was applied, some electrons would still escape the magnetic field due to anomalous electron transport/because of their high mobility. This resulted in the formation of 2 peaks in the time-varying current waveforms. The current was measured using Ohm’s law for a potential drop across a 15Ω resistor. Later, we discuss the results pertaining to negative ion current measurements in section 3.3.

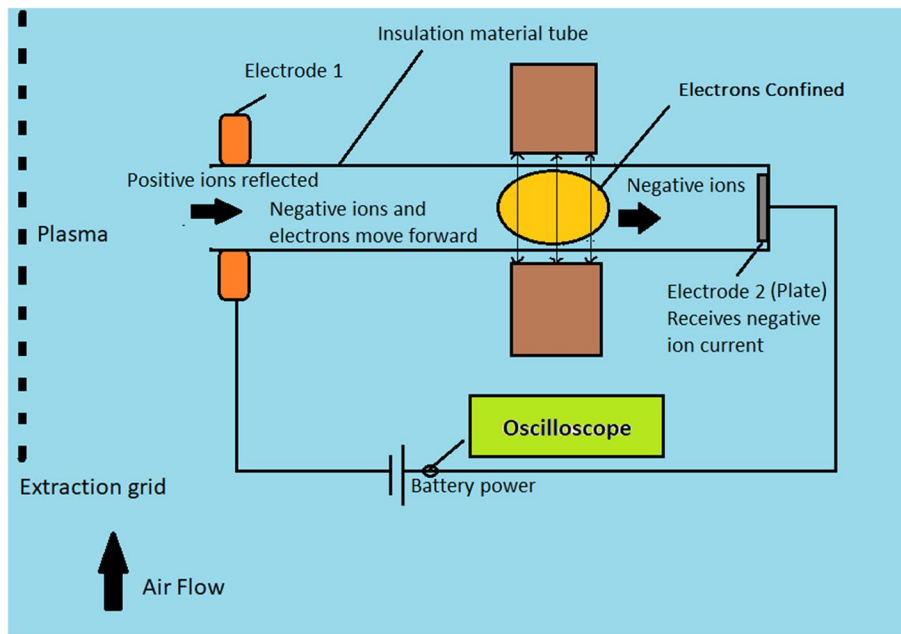


Fig. 4 The tube design for the magnetic filter. The design calculations based on eq. 3 result in the drift tube length of 50 mm for a 0.12T magnetic field. The design configuration can be observed: radial magnetic field design for electron confinement such that negative oxygen ion current was received at electrode 2. Negative charges drifted from low to high potential while the positive charges were repelled

Results

In this section, the positive and negative air ion formation by the AES were analyzed.

Plasma parameters

The ion and electron current as a function of grid voltage and pressure (mean electron energy) are presented in Fig. 5 (a-b).

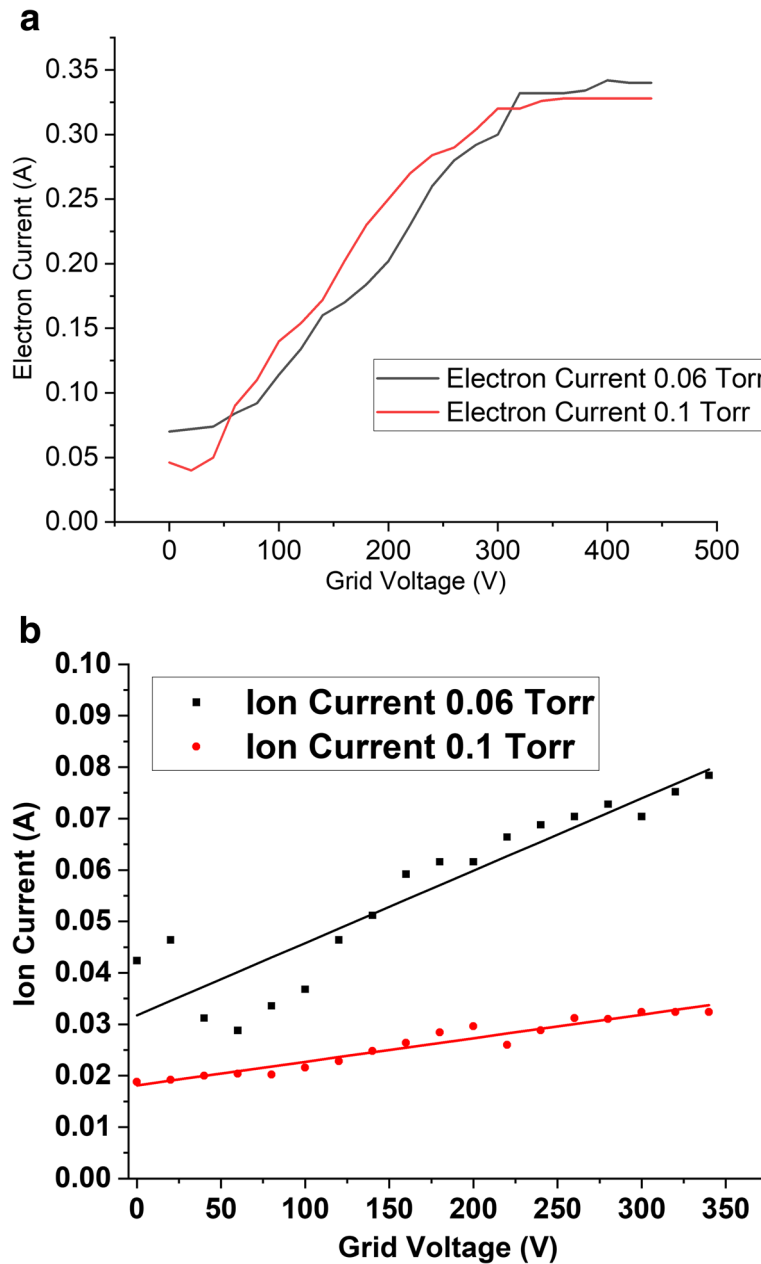


Fig. 5 The variation of electron (a) and ion (b) saturation current with grid voltage (mean electron energy) with pressure as a parameter can be seen. The distance between the grid and the vacuum arc source was 25 mm. The currents were measured using a Faraday cup biased to ± 40 V. The cup was 35 mm away from the AES. The ion current measured was the saturated current in the air. The increase in the ion current was because of an increase in the electron current with grid voltage indicating air ionization

The distance between the grid and source was set to prevent arcing and secondary electron emission in a medium pressure regime. The total ion current (saturated around -40 V) can be seen in Fig. 5(b). It increases with the extraction voltage indicating the ionization. Later we show that based on the OES data a low emission/density of vacuum source copper ions above the grid can be seen indicating air ionization. The increase in the ion current can be 2.5 (0.06 Torr) times up to 330 V.

The current-voltage characteristics measured by the Langmuir probe yield the following electron temperature values 1.82 eV, 1.15 eV, and 1.63 eV for pressures 0.05 Torr, 0.07 Torr, and 0.09 Torr, respectively. These values are typical for vacuum arc sources (1 eV–2 eV) [35]. These temperatures were calculated at the grid voltage of 0 V. Additionally, electron temperatures with grid voltages were obtained more accurately using OES results discussed in section 3.2. First, the electron temperatures were utilized to calculate the electron density. Later, the estimated electron densities were used to obtain the ion formation rate in section 3.2.

The ion current variation with the grid voltage can be observed in Fig. 6. The maximum saturated ion current and electron densities were 20.2 mA and $3.17 \times 10^{15} \text{ m}^{-3}$. These conditions were obtained at 330 V, 0.05 Torr, and 20 mm distance (Fig. 6(a)). The maximum ion currents and electron densities for 0.07 Torr and 0.09 Torr pressure conditions were 13 mA, 7.5 mA, $2.53 \times 10^{15} \text{ m}^{-3}$, $1.21 \times 10^{15} \text{ m}^{-3}$. At the 0.07 Torr and 0.09 Torr, there was airflow into the plasma chamber, whereas 0.05 Torr was the base pressure. The bias of the probe was -40 V as the saturated current was received. The increase in axial distance (between the cup and the AES) resulted in reducing the electron density. Plume expansion and attachment lead to electron density decay. The increment in the electron density with grid voltage indicated air ionization. Our earlier results [1] confirmed that the electron densities increased with the mean electron energy as the ionization reaction rate coefficient is a function of electron temperature.

OES measurements

The OES analysis was performed for 2 cases. The first case involved placing the OES probe between the vacuum arc source and the extraction grid, and for the second case, the probe was placed above the grid.

The results show the OES spectrum dominated by Cu^+ ion emissions (Fig. 7) between the grid and the vacuum arc source. When the probe was placed above the grid, the intensities for N_2^+ were more significant for the 300 V grid voltage case than 0 V. This

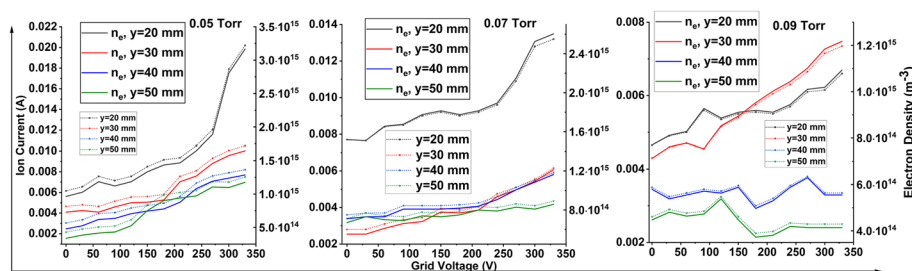


Fig. 6 Ion current along with computed electron densities as a function of the extraction grid voltage for distances 20 mm–50 mm at the pressure 0.05 Torr, 0.07 Torr, and 0.09 Torr

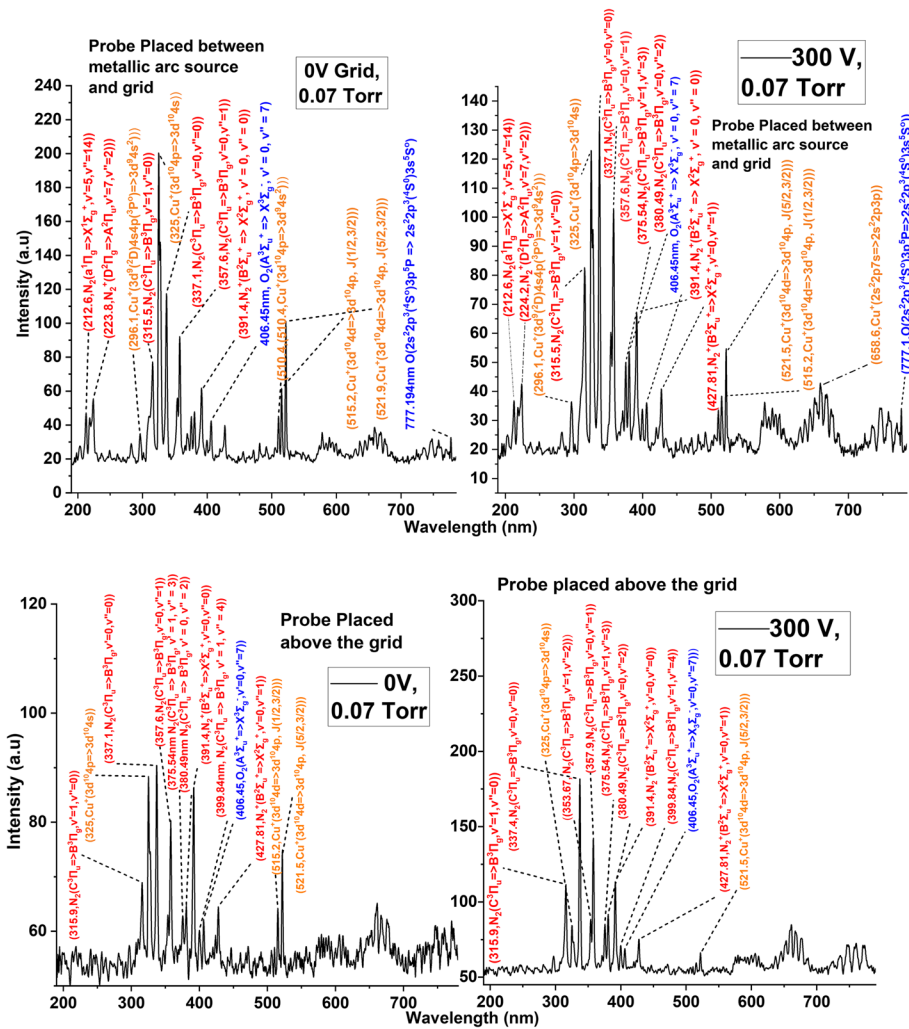


Fig. 7 The OES data (orange-Copper, red-Nitrogen, blue-Oxygen). The observed results are at 0V and 300V grid voltage for 0.07Torr chamber pressure

indicates additional ionization previously observed by the Langmuir probe. The line ratio method can determine the relation between mean electron temperature, electron density, EEDF [36], rate coefficients, and formation rate with grid voltage and pressure.

When the probe was placed above the grid, most intensities seen in Fig. 7 originate from nitrogen species as it contributes to a significant fraction of air. The transitions shown for wavelengths 337.1 nm, 357.6 nm, 315.9 nm, 375.54 nm, and 380.49 nm belong to the second positive nitrogen system ($C^3\Pi_u - B^3\Pi_g$). This system frequently occurs in arcs at low pressures (Ref. [20], refer to pg. 219). The line ratio analysis for molecules is complex due to their higher degrees of freedom. Hence, the electron temperature was obtained using the spectral lines of Cu^+ ions. The Cu^+ ion spectral lines at 325 nm and 521.5 nm that is $Cu^+(3d^{10}4p \rightarrow 3d^{10}4s)$ and $Cu^+(3d^{10}4p \rightarrow 3d^{10}4p, J(5/2, 3/2))$, were selected. These peak lines indicate closeness to ionization levels and a higher population of excited/ionized particles according to the NIST database website [19]. Equation 1 was curve fitted to obtain electron temperature

variation with grid voltage for 0.07 Torr and 0.09 Torr pressure (with airflow in the chamber). The computed results in Figs. 7, 8, 9 and 10 indicate the effect of extraction grid voltage and pressure on electron temperature, rate coefficients, and spectral line intensities. The increment in the electron temperature was seen for both 0.07 Torr and 0.09 Torr pressure conditions. The electron temperature obtained from the OES experiments ranged between 1.1 eV - 1.27 eV (Fig. 8), close to that obtained from the Langmuir probe analysis. The electron temperature increase was a clear indication of air ionization as the electron impact rate of ion formation (eqs. 2 and 4) is directly proportional to the electron temperature. The OES emission results consist of an oxygen peak (406.45 nm, $A^3\Sigma_u^+ \Rightarrow X^3\Sigma_g^-, v'=0, v''=7$) of a special interest and it is shown in Fig. 9. The O_2 (406.45 nm, $A^3\Sigma_u^+ \Rightarrow X^3\Sigma_g^-, v'=0, v''=7$) emission line indicates the Herzberg System [20] that exists generally at high pressures in air plasma discharges.

The OES experiments were conducted for 0.07 Torr – 0.5 Torr pressure ranges for grid voltages of 0V–6V to potentially prove the presence of O^- ions in the air plasma. The lower voltage ranges were selected because the attachment rate coefficients dominate the ionization rates in mean electron energies less than 5 eV [1]. Based on Fig. 9(a), the peak intensity of 88 (a.u) was seen at the pressure of 0.15 Torr for the oxygen emission line. Additionally, experiments were conducted at 0.15 Torr pressure for 0V–300V grid voltages. In the lower voltages (<4V), the emission intensity reduces (potentially due to electron attachment to oxygen) and then increases from 5V – 300V, indicating ionization.

Based on measured electron temperature and electron density one can calculate the rate of formation [1] of the ion through electron impact:

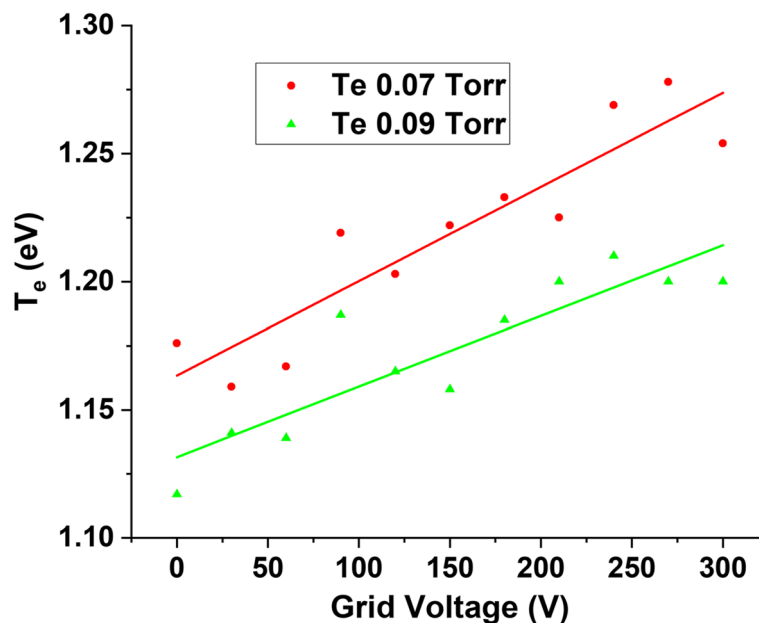


Fig. 8 The results show the electron temperature as a function of grid voltage and pressure obtained from the OES

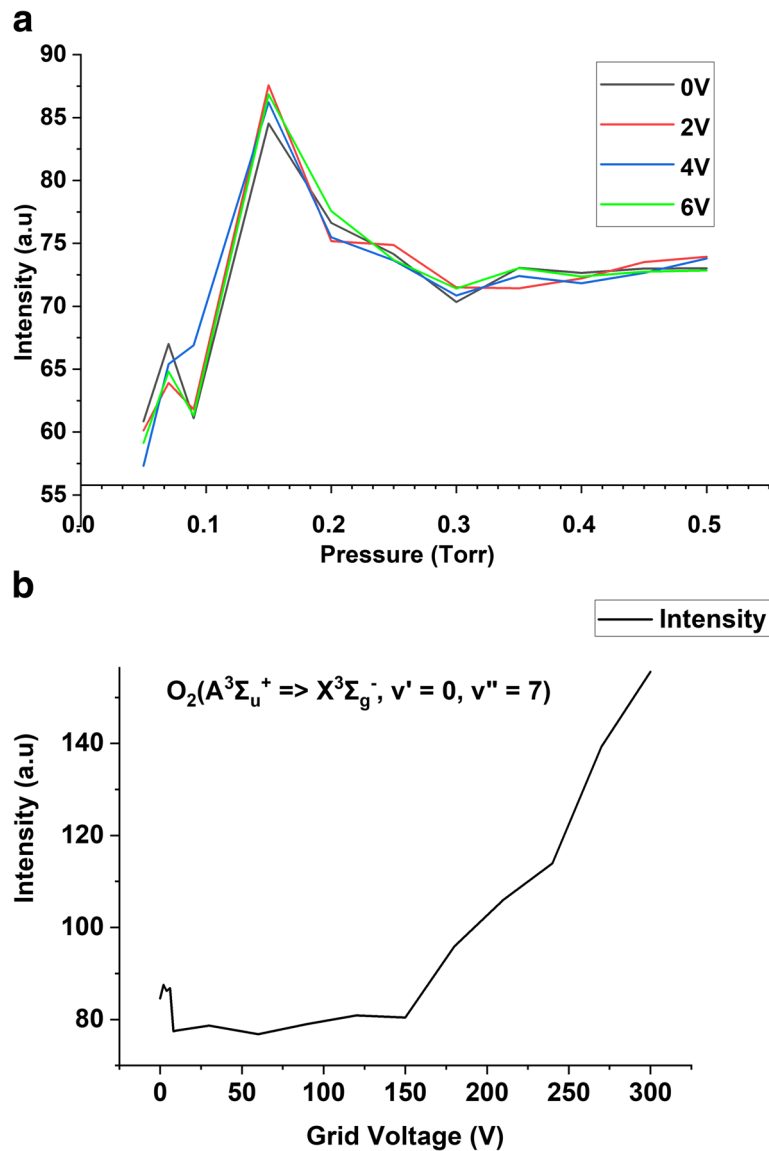


Fig. 9 The results for O₂ (406.45 nm, A³Σ_u⁺ => X³Σ_g⁻, v'=0, v''=7) emission line is shown. The oxygen emission peaks at 0.15Torr pressure (a) at a grid voltage range of 0V - 6V. The intensity of O₂ initially reduces up to 4V (b) and then increases with the grid voltage

$$R_f = k_k n_e n_n \tag{4}$$

where, R_f , n_e and n_n are the rate of ion formation (s^{-1}), electron, and neutral density (N₂ or O₂, m⁻³). The results for R_f can be seen in Fig. 10 for attachment and ionization reactions. The rate coefficients were obtained from the electron temperature (as a function of grid voltage from the OES results) and solving eq. 2. The N₂ and O₂ neutral density for the 0.07 Torr and 0.09 Torr were utilized to calculate the ion rate formation. These were calculated based on the ideal gas law (gas temperature 300 K) as $2.22 \times 10^{21} m^{-3}$ and $2.86 \times 10^{21} m^{-3}$.

The electron density at 20 mm distance from Faraday cup experiments section 3.1 for 0.07 Torr and 0.09 Torr was used for calculations. The formation rate can be utilized to

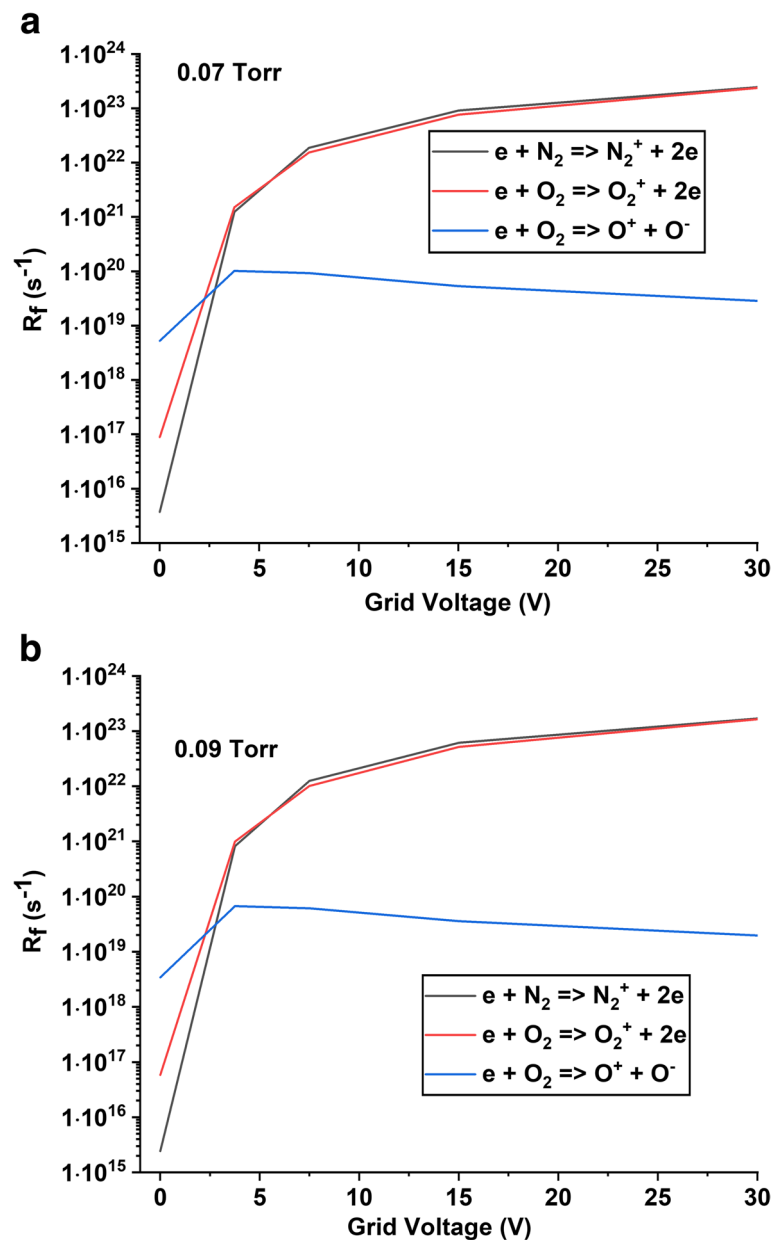


Fig. 10 The formation rate for N_2^+ , O_2^+ , and O^- vs. grid voltage at 0.07Torr (a) and 0.09Torr (b)

study the special-temporal evolution of ion/electron number densities in plasma by solving the chemical kinetics eq. [1]. Typically, ionization reaction rate coefficients increase with mean electron energy and vice versa for attachment reactions. It can be seen that the O^- ion formation from the Fig. 10 is more significant (<5 V) than positive ions as the electron impact collision cross-sections for the dissociative electron attachment reactions peak in lower electron energies (<2.5 eV). The electron attachment reaction occurred due to dissociative attachment [12]. Therefore, the formation of negative ions due to oxygen's electronegativity could be used as an advantage to achieve charge neutralization with positive ions for the SABPT, as previously described [1]. In conclusion, the electron temperature and formation rate obtained using OES indicated ionization

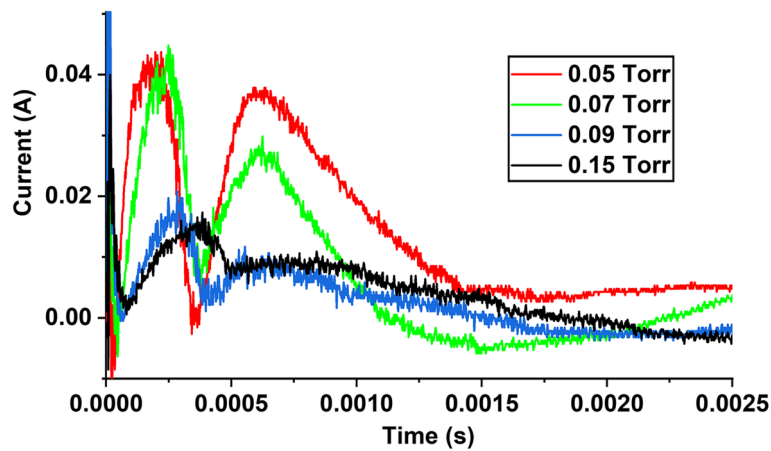


Fig. 11 Current waveforms with pressure as a parameter

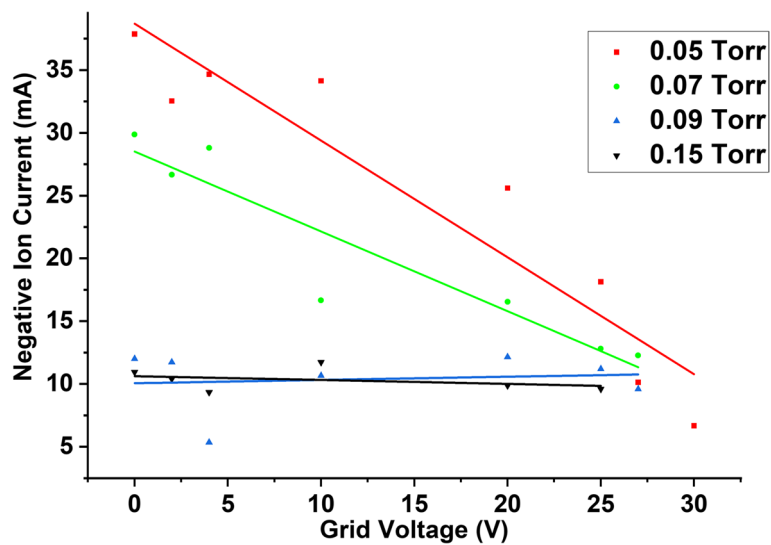


Fig. 12 Negative ion current peak as a function of grid voltage at different pressures

and electron attachments (negative ion formation) as a function of grid voltage and pressure. In the following section, we describe a magnetic filter drift tube to characterize negative ion formation.

Magnetic filter measurements

Negative ion current measurements are shown in Fig. 11 and Fig. 12. The temporally varying current waveforms indicated two peaks. The first peak is likely due to electrons, while the second peak corresponds to negative ions. The peaks for negative ion current were observed below 5 V grid voltage. Consequently, with rising grid voltage, the negative ion current is reduced (due to ionization, recombination, and electron detachment) as shown in Fig. 10. The peak negative ion current was seen around 40 mA (0.05 Torr), more significant than the positive ion current.

Earlier, (Fig. 2 Ref. [1]) it was observed that the coefficient for the attachment was more significant than the ionization reaction below 5 eV temperature. The plasma temperature obtained from the experiments was in the 1 eV–2 eV range. Therefore, the temperature was not high enough to create higher ionization. Additionally, the grid voltage was below 5 V (mean electron temperature); we see a more significant negative ion current than a positive ion current. Figure 11 shows the temporal variation of negative ion current waveforms as a function of chamber pressure (0.05 Torr–0.15 Torr) for 0 V grid voltage. Figure 12 shows the linear fit negative ion current variation as a function of grid voltage (0 V–30 V) and chamber pressure (0.05 Torr–0.15 Torr).

As previously discussed, the SABPT [1] would operate by controlling the mean electron energy of the electron source to produce positive and negative ions. The proposed electron source for the SABPT design (AES) contained an electron extraction grid that could potentially be pulsed in the range of 0 V–300 V to produce maximum positive and negative ion densities. Furthermore, quantitative analysis based on experimental results has been described in the next section.

Concluding remarks

This study aimed to characterize a magnetic field-enhanced AES for air ionization applications inside a SABPT. It was designed using a vacuum arc plasma source coupled with an electron extraction grid. The grid-enabled the control of the mean electron energy. Experimentally, it was shown that the positive ion current, electron current, electron density, and electron temperature increased with an increment in the grid voltage. On the contrary, the measured negative ion current reduced with the grid voltage. Furthermore, a combination of Langmuir probe/Faraday cup, OES, and magnetic filter tube plasma diagnostics enabled us to characterize the AES.

The mechanism of SABPT involves alternating the electron energy of an electron source to create positive and negative ions to achieve self-neutralization. It has been shown that the negative oxygen ion formation rate was higher in the case of low electron energy (1 eV–2 eV) while high electron energy leads to a higher positive ion formation rate. It was obtained that the maximum positive and negative ion currents are 20.2 mA and 40 mA respectively, the electron density is about $3 \times 10^{15} \text{ m}^{-3}$, and the electron temperature is about 1.1–1.2 eV. Presented experimental results suggest that conditions for the self-neutralizing air-breathing plasma thruster proposed theoretically can be achieved. Further scaling up of the system in power and size is needed to produce thrust for VLEO application.

Authors' contributions

All authors contributed to the study, conception, and design. The first draft of the manuscript was written by Anmol Taploo and all authors commented on previous versions of the manuscript. All authors read and approved the final manuscript.

Funding

The work was supported by an Air Force Office of Scientific Research, FA9550-19-1-0166 (Dr. Mitat Birkan is the program manager) and NASA through DCSGC.

Declarations

Consent for publication

All authors gave their explicit consent to submit the content of this article for publication in the Springer Journal of Electric Propulsion.

Competing interests

The authors have no competing interests to declare that are relevant to the content of this article.

Received: 27 June 2022 Accepted: 24 October 2022

Published online: 17 November 2022

References

1. Taploo A, Lin L, Keidar M (2021) Analysis of ionization in air-breathing plasma thruster. *Phys Plasmas* 28:093505. <https://doi.org/10.1063/5.0059896>
2. Ferrato, Giannetti, Piragino, Andrenucci and Andreussi, Development Roadmap of SITAELs RAM-EP System, (2019). <http://electricrocket.org/2019/886.pdf>
3. Pekker L, Keidar M (2012) *J Propuls Power* 28:1399. <https://doi.org/10.2514/1.B34441>
4. Neil Wallace, Jameson, Saunders, Fehring, Edwards and Floberghagen, the GOCE ion propulsion assembly – lessons learnt from the first 22 months of flight operations, (2011). <http://electricrocket.org/IEPC/IEPC-2011-327.pdf>
5. Pulsed metallic-plasma generators. *IEEE Xplore* (n.d.). Retrieved January 27, 2022, from <https://ieeexplore.ieee.org/abstract/document/1450751>
6. Zhuang T, Shashurin A, Denz T, Keidar M, Vail P, Pancotti A (2014) Performance characteristics of micro-cathode arc thruster. *J Propuls Power* 30(1):29–34. <https://doi.org/10.2514/1.B34567>
7. BRICSAT-P - satellite missions - eoportal directory. P. (n.d.). Retrieved January 27, 2022, from <https://directory.eoportal.org/web/eoportal/satellite-missions/content/-/article/bricsat-p>
8. Magnetically enhanced vacuum arc thruster - iopscience. (n.d.). Retrieved January 27, 2022, from <https://iopscience.iop.org/article/10.1088/0963-0252/14/4/004>
9. Efim M (1999) Oks, "Development of plasma cathode electron guns". *Phys Plasmas* 6:1649–1654. <https://doi.org/10.1063/1.873420>
10. Zolotuchin DB, Banduru RSP, Daniels KP, Beilis II, Keidar M (2022) Demonstration of electric micro-propulsion multimodality. *Sci Adv* 8:eac9850
11. Lun J (2009) Development of a vacuum arc thruster for nanosatellite propulsion, pp 4–6 <http://hdl.handle.net/10019.1/1527>
12. Munro JJ, Harrison S, Fujimoto MM, Tennyson J (2012) *J Phys Conf Ser* 388:012013
13. Martins, A., Pinheiro, M. (2011). On the propulsive force developed by asymmetric capacitors in a vacuum. Retrieved May 24, 2022, from <https://www.sciencedirect.com/science/article/pii/S1875389211005797?via%3Dihub>
14. Zhuang T, Shashurin A, Keidar M, Beilis II (2011) Circular periodic motion of plasma produced by a small-scale vacuum arc. *Plasma Sources Sci Technol* 20(1):015009. <https://doi.org/10.1088/0963-0252/20/1/015009>
15. Rysanek, F., Hartmann, J., Schein, J., Binder, R. (1970). Microvacuum arc thruster design for a cubesat class satellite: Semantic scholar undefined Retrieved January 27, 2022, from <https://www.semanticscholar.org/paper/Micro-vacuum-Arc-Thruster-Design-for-a-Cubesat-Class-Rysanek-Hartmann/1a47b6e7ffc9ecc1926b3db0de121743ef08d280>
16. G. Teel, J. Lukas, A. Shashurin, M. Keidar, "Analysis of Ignition of the Micro Cathode Arc Thruster", *IEPC-53* (2015); http://electricrocket.org/IEPC/IEPC-2015-53_IJTS-2015-b-53.pdf
17. StellarNet Inc. Retrieved January 27, 2022, from <https://www.stellar.net.us/spectrometers/hr-high-resolution-spectrometers/>
18. Finite element method magnetics - femm.info. (n.d.). Retrieved January 27, 2022, pp. 6–8, from <https://www.femm.info/Archives/doc/manual42.pdf>
19. Atomic spectra database lines form. NIST. (n.d.). Retrieved January 27, 2022, from https://physics.nist.gov/PhysRefData/ASD/lines_form.html
20. B., P. R. W. Gaydon, A. G. (1976). *The identification of molecular spectra*. 4. Ed.
21. Chen, C., Fu, W., Zhang, C., Lu, D., Han, M., Yan, Y. (2020). Langmuir probe diagnostics with optical emission spectrometry (OES) for coaxial line microwave plasma. *Applied sciences*, 10(22), 8117. <https://doi.org/https://doi.org/10.3390/app10228117>
22. Zhang Y, Yi X, Zhang Z, Liu Z, Geng Y, Wang J, Wang W, Li G, Wang X (2016) Electron temperature and electron density of copper vacuum arc in diffuse arc mode and anode spot arc mode. 2016 27th international symposium on discharges and electrical insulation in vacuum (ISDEIV). <https://doi.org/10.1109/deiv.2016.7748736>
23. Keidar M, Beilis II (2013) *Plasma engineering: applications from aerospace to bio- and nanotechnology*. Academic Press, p 336 <https://www.elsevier.com/books/plasma-engineering/keidar/978-0-12-385977-8>
24. Hagelaar GJM, Pitchford LC (2005) solving the Boltzmann equation to obtain electron transport coefficients and rate coefficients for fluid models, *plasma sources Sci. Technol* 14:722–733 <https://iopscience.iop.org/article/10.1088/0963-0252/14/4/011>
25. Boffard JB, Jung RO, Lin CC, Wendt AE (2010) Optical emission measurements of electron energy distributions in low-pressure argon inductively coupled plasmas. *Plasma Sources Sci Technol* 19(6):065001. <https://doi.org/10.1088/0963-0252/19/6/065001>
26. Plasma module application library manual - COMSOL documentation. (n.d.). Pg. 184. Retrieved may 24, 2022, from <https://doc.comsol.com/5.3/doc/com.comsol.help.plasma/PlasmaApplicationLibraryManual.pdf>
27. BOLSIG Solver. Bolsig+. (n.d.). Retrieved January 27, 2022, from <http://www.bolsig.laplace.univ-tlse.fr/index.html>
28. LXcat, see <https://nl.lxcat.net/home/> for "cross-sections data of nitrogen and oxygen" (2020)
29. Stoffels E, Stoffels WW, Vender D, Kando M, Kroesen GM, De Hoog FJ (1995) Negative ions in a radio-frequency oxygen plasma. *Phys Rev E* 51(3):2425–2435. <https://doi.org/10.1103/physreve.51.2425>
30. Hayashi D, Kadota K (1998) Measurements of negative ion density in high-density oxygen plasmas by probe-assisted laser Photodetachment. *J Appl Phys* 83(2):697–702. <https://doi.org/10.1063/1.366740>

31. McKnight LG (1970) Drift velocities and interactions of negative ions in oxygen. *Phys Rev* 2(3):762–770. <https://doi.org/10.1103/physrev.2.762>
32. Mieno T, Kamo T, Hayashi D, Shoji T, Kadota K (1996) Efficient production of O⁺ and O[−] ions in a helicon wave oxygen discharge. *Appl Phys Lett* 69(5):617–619. <https://doi.org/10.1063/1.117925>
33. Zhang A, Kwon D-C, Chung C-W (2020) A method for measuring negative ion density distribution using harmonic currents in a low-pressure oxygen plasma. *Plasma Sources Sci Technol* 29(6):065017. <https://doi.org/10.1088/1361-6595/ab9485>
34. Modeling of air plasma generation by repetitive high-voltage nanosecond pulses. *IEEE Xplore*. (n.d.). Retrieved May 31, 2022, from, <https://ieeexplore.ieee.org/stamp/stamp.jsp?tp=&arnumber=1158293&tag=1>
35. Keidar M et al (2005) *Plasma Sources Sci. Technol* 14:661 <https://iopscience.iop.org/article/10.1088/0963-0252/14/4/004/meta>
36. Fantz U (2006) Basics of plasma spectroscopy. *Plasma Sources Sci Technol* 15(4). <https://doi.org/10.1088/0963-0252/15/4/s01>

Publisher's Note

Springer Nature remains neutral with regard to jurisdictional claims in published maps and institutional affiliations.